Applied Physics Letters

RESEARCH ARTICLE | JUNE 01 2023

Ferroelectric behavior of sputter deposited $Al_{0.72}Sc_{0.28}N$ approaching 5 nm thickness

Jeffrey X. Zheng ; Merrilyn Mercy Adzo Fiagbenu ; Giovanni Esteves ; Pariasadat Musavigharavi ; Akhil Gunda ; Deep Jariwala ; Eric A. Stach ; Roy H. Olsson, III

Check for updates

Appl. Phys. Lett. 122, 222901 (2023)
https://doi.org/10.1063/5.0147224

View Online
Export Citation
CrossMark

AIP Publishing

Applied Physics Letters ARTICLE pubs.aip.org/aip/apl

Ferroelectric behavior of sputter deposited $Al_{0.72}Sc_{0.28}N$ approaching 5 nm thickness

Cite as: Appl. Phys. Lett. **122**, 222901 (2023); doi: 10.1063/5.0147224
Submitted: 20 February 2023 · Accepted: 17 May 2023 ·
Published Online: 1 June 2023

Jeffrey X. Zheng,[1] Merrilyn Mercy Adzo Fiagbenu,[2] Giovanni Esteves,[3] Pariasadat Musavigharavi,[1,2] Akhil Gunda,[2] Deep Jariwala,[2] Eric A. Stach,[1,4] and Roy H. Olsson III[2,a)]

AFFILIATIONS

[1] Department of Materials Science and Engineering, University of Pennsylvania, Philadelphia, Pennsylvania 19104, USA
[2] Department of Electrical and Systems Engineering, University of Pennsylvania, Philadelphia, Pennsylvania 19104, USA
[3] Microsystems Engineering, Science and Applications, Sandia National Laboratories, Albuquerque, New Mexico 87123, USA
[4] Laboratory for Research on the Structure of Matter, University of Pennsylvania, Philadelphia, Pennsylvania 19104, USA

[a)] Author to whom correspondence should be addressed: rolsson@seas.upenn.edu

ABSTRACT

Ferroelectric $Al_{1-x}Sc_xN$ has raised much interest in recent years due to its unique ferroelectric properties and complementary metal oxide semiconductor back-end-of-line compatible processing temperatures. Potential applications in embedded nonvolatile memory, however, require ferroelectric materials to switch at relatively low voltages. One approach to achieving a lower switching voltage is to significantly reduce the $Al_{1-x}Sc_xN$ thickness. In this work, ferroelectric behavior in 5–27 nm films of sputter deposited $Al_{0.72}Sc_{0.28}N$ has been studied. We find that the 10 kHz normalized coercive field increases from 4.4 to 7.3 MV/cm when reducing the film thickness from 27.1 to 5.4 nm, while over the same thickness range, the characteristic breakdown field of a 12.5 μm radius capacitor increases from 8.3 to 12.1 MV/cm. The 5.4 nm film demonstrates ferroelectric switching at 5.5 V when excited with a 500 ns pulse and a switching speed of 60 ns.

Overcoming the von Neumann memory bottleneck calls for a fast and low energy interface between memory and compute, which can be accomplished via monolithic integration of dense, fast nonvolatile memory (NVM) and silicon complementary metal oxide semiconductor (CMOS) microprocessors.[1,2] Ferroelectric memories that can be embedded in the (CMOS) back-end-of-line (BEOL) are an interesting solution to the memory bottleneck because of their low switching energy,[3] fast switching speed,[4] and potential for multibit operation.[5] Ferroelectric $Al_{1-x}Sc_xN$ is a promising material for BEOL ferroelectric memory owing to its unique ferroelectric properties and low temperature deposition and processing.[6,7] Recently, the thickness scaling of $Al_{1-x}Sc_xN$ has been studied down to thicknesses of 25,[8] 20,[9] 15,[10] 10,[11] and 9 nm (Ref. 12) in sputter deposited films and to 5 nm (Ref. 13) in films deposited by molecular beam epitaxy (MBE).

This work adds to the body of research and studies the ferroelectric and dielectric properties of sputter deposited $Al_{0.72}Sc_{0.28}N$ through the deposition and characterization of films ranging from 27.1 to 5.4 nm thickness on Al templates grown on Sapphire substrates. The underlying template is incredibly important for forming highly c-axis oriented $Al_{1-x}Sc_xN$ thin films via sputtering. The underlying template should present hexagonal symmetry preferably with a hexagonal close pack (hcp) spacing similar to the a-axis lattice constant of $Al_{1-x}Sc_xN$. From previous works,[14,15] $\langle 111 \rangle$ Al is a known template for c-axis oriented $Al_{1-x}Sc_xN$ and a metal that can be deposited at low temperatures for embedded NVM. In addition to lattice matching between the template and $Al_{1-x}Sc_xN$, another important consideration is the crystal quality and roughness of the template. Sapphire wafers were chosen because of the lattice matching between sapphire and Al. This allowed for the deposition of highly oriented $\langle 111 \rangle$ Al bottom electrodes and relatively well oriented $Al_{1-x}Sc_xN$ films down to 5.4 nm. The high thermal boundary conductance between Al and sapphire[16] prevents local temperature spikes that lead to hillock formation in Al layers, which results in premature electrical breakdown in thin $Al_{1-x}Sc_xN$ films. This work provides x-ray diffraction (XRD) data to show the crystallinity of said films as well as electrical characterization, showing the ferroelectric switching behavior of the films under 500 ns voltage pulses. Leakage and breakdown strength are also evaluated. Finally, the results are compared with other published work to show the trend in $Al_{1-x}Sc_xN$ properties with decreasing thickness.

Stacks of Al (46 nm)/$Al_{0.72}Sc_{0.28}N$/Al (46 nm) were deposited on 100 mm c-axis (0.2° +/− 0.1° to M-plane) oriented sapphire wafers using physical vapor deposition (PVD). The sputter deposition of all films was completed without breaking vacuum using an Evatec CLUSTERLINE® 200 II PVD system with a target-to-substrate distance of 88.5 mm. Al layers are deposited as top and bottom electrode layers used for testing the ferroelectric and dielectric properties of the $Al_{0.72}Sc_{0.28}N$ layers. The ⟨111⟩ Al is deposited at 150 °C with an Al target power density of 12.7 W/cm^2 under 20 sccm Ar flow resulting in a process pressure of 1.1×10^{-3} mbar. The deposition rate of the Al was 1.3 nm/s. The $Al_{0.72}Sc_{0.28}N$ layer is deposited on the bottom layer of Al via co-sputtering at 350 °C with an Al target power density of 11.1 W/cm^2, a Sc target power density of 7.07 W/cm^2, and 20 sccm of N_2 flow that results in a process pressure between 8×10^{-4} and 8.5×10^{-4} mbar. The various $Al_{0.72}Sc_{0.28}N$ thicknesses were achieved by adjusting the deposition time using a deposition rate of 0.25 nm/s. Al top electrodes were patterned with an Oxford PlasmaPro 100 Cobra inductively coupled plasma (ICP) etcher, while the bottom electrodes of all the specimens were exposed by wet etching the AlScN film with 30 mol. % KOH solution.

The $Al_{0.72}Sc_{0.28}N$ thicknesses were measured to be 27.1, 18.1, 14.0, 9.6, and 5.4 nm ± 1 nm via x-ray reflectometry (XRR). XRR fits were performed with GSAS-II,[17] which uses an optical matrix method as its model. The layer stack used in model refinement consisted of alumina-sub/Al-BE/$Al_{0.72}Sc_{0.28}N$/Al-TE/alumina-NL, where alumina-sub is the sapphire substrate, Al-BE is the Al bottom electrode, Al-TE is the Al top electrode, and alumina-NL is the native oxide layer that forms on Al films exposed to atmosphere. The density of $Al_{0.72}Sc_{0.28}N$[18] used was 3.31 g/cm^3. The fit for the 5.4 nm $Al_{0.72}Sc_{0.28}N$ film (Fig. S1) and all the refined values for the other film stacks are shown in the supplementary material. The XRR fit includes the measured and calculated data in addition to the refined $Al_{0.72}Sc_{0.28}N$ films' contribution to the XRR. The fringes from the 5.4 nm $Al_{0.72}Sc_{0.28}N$ film can be seen to match the measured XRR data, which gives confidence in the least squares refinement of the multi-layer model. The ± 1 nm error bars in the thickness measurements represent variations in the least squares routine from multiple refinement approaches of the XRR pattern. The thicknesses determined by XRR shown in supplementary material Table 1 are utilized for all coercive and breakdown field calculations.

Scanning/transmission electron microscopy (S/TEM) characterization and image acquisition were carried out on a JEOL F200 TEM operated at 200 kV accelerating voltage. TEM cross-sectional samples of the AlScN film were prepared by a plasma-focused ion beam (TESCAN S8000X PFIB-SEM) system using the *in situ* lift-out technique. The sample was coated with ion beam deposition of Pt protection layers to prevent charging and heating effects during FIB milling. All quantification results presented in this work were calculated with Digital Micrograph software (DM, Gatan Inc., USA). Shown in Fig. 1(a) is a cross-sectional Transmission Electron Microscope (TEM) image of an Al/$Al_{0.72}Sc_{0.28}N$/Al film targeting 5 nm $Al_{0.72}Sc_{0.28}N$ thickness using the same sputtering conditions as the films studied electrically in this work. Due to limitations in preparing TEM samples on sapphire substrates utilizing a plasma-focused ion beam, the TEM sample was prepared on a silicon substrate, and a 100 nm thick $Al_{0.72}Sc_{0.28}N$ film was used as a template for the growth of the ⟨111⟩ Al bottom electrode. The Si substrate is oriented along the (001) crystallographic direction, and the interface between the layers is indicated by white dashed lines. The high-resolution TEM image in Fig. 1(b) reveals sharp interfaces between the Al/$Al_{0.72}Sc_{0.28}N$/Al layers. It is clearly visible that by growing the entire film stack without vacuum break, no interlayers are observed between the Al electrodes and the $Al_{0.72}Sc_{0.28}N$ film. Figure 1(c) shows a bright-field STEM image of the material stack. The EDS mapping of the region enclosed by the white box shows the distribution of elements in the film, indicating the presence of Al and Sc with the expected spatial variation. The scale bar in the insets of Fig. 1(c) corresponds to 20 nm and confirms that the $Al_{0.72}Sc_{0.28}N$ thickness is approximately 5 nm, in agreement with the XRR measurements.

XRD was completed using a PANalytical X'Pert[3] MRD diffractometer that used a Ge (220) double-bounce hybrid monochromator and a PIXcel^{3D}. The AlScN (0002) was fitted with a Pearson VII profile and the Al peak with two profiles of Gaussian and Lorentzian functions. Error bars for the refined least squares parameters are the 95% confidence interval. XRD showing θ–2θ peaks of $Al_{0.72}Sc_{0.28}N$ at various thicknesses is shown in Fig. 2(a). Sapphire has a slightly distorted oxygen sublattice, where Al occupies 2/3 of the octahedral interstitial sites with a lattice parameter of $a_{ox} = \frac{a_{Al_2O_3}}{\sqrt{3}} = 2.746$ Å.[19] This results in sapphire being an ideal heteroepitaxial substrate for materials such as Al with atomic spacing of d = 2.85 Å in the ⟨111⟩ direction. As such, using sapphire wafers allows for highly textured ⟨111⟩ Al films with an ω scan rocking curve full-width-half-maximum (FWHM) between 0.12° and 0.15° for the bottom Al layer as shown in Fig. 2(b) by the green-dashed line that represents the Lorentzian fit. The surface of these films is hillock free compared to the Al bottom electrodes grown on $Al_{0.80}Sc_{0.20}N$ seed layers on a Si substrate.[14] The thermal conductance between the Al and sapphire[16] reduces the local fluctuations of temperature in the bottom Al during the $Al_{0.72}Sc_{0.28}N$ growth at 350 °C, allowing for smooth, hillock free Al layers. The maximum processing temperature of 350 °C facilitates future CMOS BEOL integration.

The $Al_{0.72}Sc_{0.28}N$ layer shows a peak shift in the 2θ and ω scans toward lower angles as the film becomes thinner, indicating that the films, on average, become more compressive for thinner layers due to interfacial stresses.[20] The Al atomic spacing, at d = 2.85 Å, is smaller than the lattice parameter of $Al_{0.72}Sc_{0.28}N$, which is a = 3.2 Å.[21] $Al_{0.72}Sc_{0.28}N$ at the bottom electrode interface templates from the smaller Al atomic spacing and exhibits large in-plane compressive stress, which manifests as out-of-plane tensile stress due to Poisson's ratio. Figure 2(c) shows the average *c* lattice constant for the $Al_{0.72}Sc_{0.28}N$ vs thickness showing the increased out-of-plane tensile strain in the films with reduced thickness. The XRD omega scans for the $Al_{0.72}Sc_{0.28}N$ for each thickness were also performed (see Fig. S2 in the supplementary material). A wider FWHM for the $Al_{0.72}Sc_{0.28}N$ is observed with thickness scaling. The 5 nm thick film has a FWHM of 4.44° and is 0.92° greater than the value for the 27 nm film of 3.52°. The films reported in this work below 10 nm thickness are suspected of having a higher crystallinity than $Al_{1-x}Sc_xN$ films previously reported in the literature, where at 9 and 5 nm thicknesses, the XRD peaks were unobservable.[13,22]

Electrical characterization was performed using a Keithley 4200A-SCS analyzer. All tests were completed by voltage driving the capacitors from the bottom electrodes and current/charge sensing on the top electrodes. The electric breakdown fields (E_{BD}) of the films

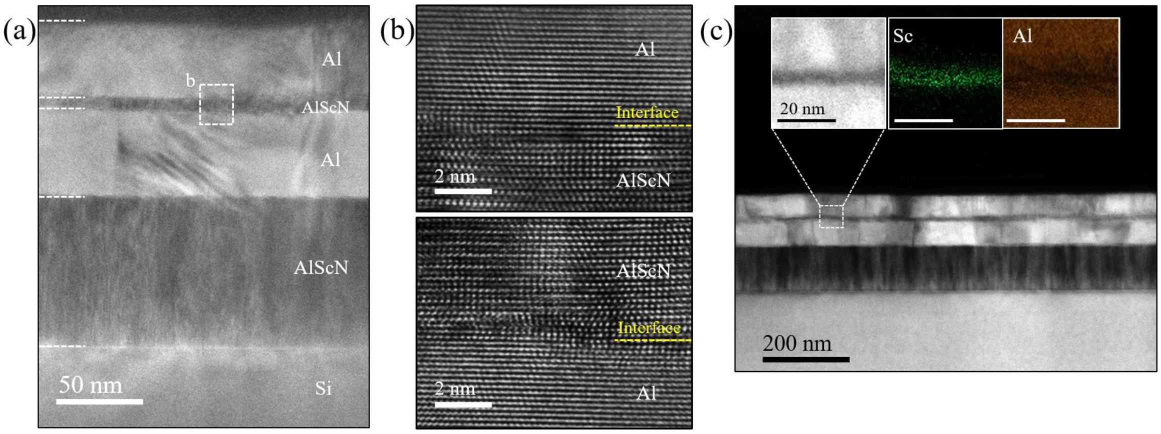

FIG. 1. (a) The cross-sectional TEM image (g = 001 Si substrate) of ~5 nm $Al_{0.72}Sc_{0.28}N$ film grown on an Al/$Al_{0.72}Sc_{0.28}N$ template on a Si substrate. The interfaces between layers are indicated by the white dashed lines. (b) High-resolution TEM image of top and bottom Al/$Al_{0.72}Sc_{0.28}N$/Al interfaces showing sharp interfaces without any interfacial layers. (c) The bright-field STEM image of the $Al_{0.72}Sc_{0.28}N$ film followed by energy dispersive x-ray spectroscopy (EDS) mapping of the region enclosed by the white box. The scale bar in the EDS mapping corresponds to 20 nm and confirms an $Al_{0.72}Sc_{0.28}N$ thickness of ~5 nm.

were measured under a 10 kHz triangular voltage waveform and recorded for the voltage, V_{BD}, at which the Keithley reached a preset current compliance limit. The Weibull analysis of the E_{BD} uses up to 20 V_{BD} measurements from pristine capacitors randomly picked across the wafer. Figure 3(a) shows the Weibull analysis of E_{BD} for 27 nm thick $Al_{0.72}Sc_{0.28}N$ as the capacitor radius is reduced from 125 to 12.5 μm, while Fig. 3(b) shows the Weibull analysis of E_{BD} for 12.5 μm radii capacitors as the film thickness is reduced from 27 to 5 nm. Both figures show a substantial increase in the E_{BD} with reduced capacitor volume, suggesting that the E_{BD} in $Al_{0.72}Sc_{0.28}N$ could be defect limited and that E_{BD} could continue to increase with further thickness scaling. Reducing the capacitor volume also tightens the

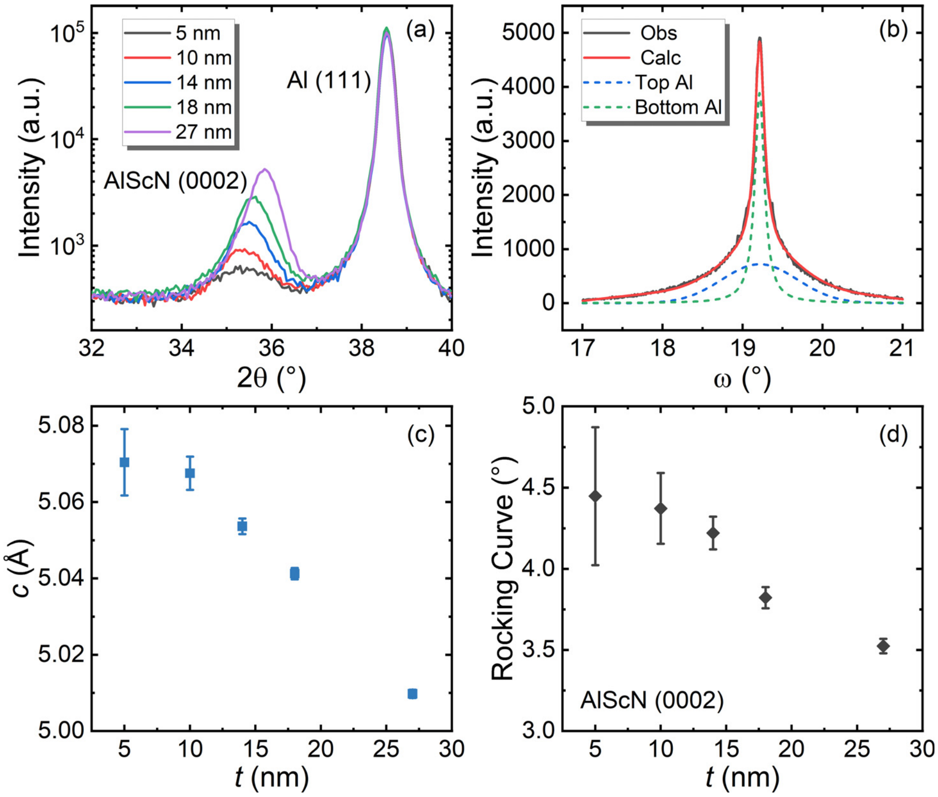

FIG. 2. (a) $\theta/2\theta$ scan showing 100 nm Al (111) and $Al_{0.72}Sc_{0.28}N$ (0002) diffraction peaks for layer thicknesses of 27, 18, 14, 10, and 5 nm, respectively. (b) ω scan of Al (111) diffraction peak showing a FWHM of ~0.14° for the bottom electrode Al and 1.11° for the top Al. (c) $Al_{1-x}Sc_xN$ average c lattice parameter vs film thickness. (d) Rocking curve ω-scan FWHM of $Al_{1-x}Sc_xN$ (0002) vs thickness.

distribution of breakdown failure, leading to improved reliability. The 5 nm thick $Al_{0.72}Sc_{0.28}N$ reaches a 10 kHz characteristic breakdown field of 12.1 MV/cm, among the highest observed for thin-film, BEOL compatible dielectric materials.

Quasi-DC (∼0.01 Hz) I–V hysteresis measurements of 12.5 μm radius capacitors are performed to assess the material leakage as a function of thickness and are shown in Figs. 3(c) and 3(d). The DC leakage current density for a given electric field is seen to decrease with decreasing film thickness. Ferroelectric behavior can be observed in the $Al_{0.72}Sc_{0.28}N$ films using the quasi-DC measurements from the change in film resistance upon ferroelectric switching.[23]

The $Al_{0.72}Sc_{0.28}N$ ferroelectric properties were characterized via current density–electric field (J–E) hysteresis loops and positive-up-negative-down (PUND) measurements. J–E hysteresis loops were measured with a triangular voltage excitation at 10 kHz for the 27 and 18 nm samples and at 100 kHz for the 10 and 5 nm samples. PUND measurements were taken using 500 ns square wave pulses with a rise/fall time of 135 ns and an inter-pulse delay time of 10 μs. Profiles for both measurements are shown in Fig. S3. To verify full ferroelectric switching on the first pulse (i.e., P and N), the 500 ns PUUNDD waveform with an inter-pulse delay time of 10 μs shown in Fig. S3(c) is also utilized. The 10 kHz E_C^+/E_C^- for the 27 and 18 nm thick $Al_{0.72}Sc_{0.28}N$ materials was found to be 5.4/−4.9 and 6.3/−5.3 MV/cm from the peaks in the J–E hysteresis loops measured on 12.5 μm radius capacitors shown in Fig. S4. As shown in Fig. S4, $Al_{0.72}Sc_{0.28}N$ films with thickness below 18 nm, while exhibiting hysteresis, did not show distinct ferroelectric peaks in the J–E hysteresis loops, and the E_C could not be determined from the measurements. PUND and PUUNDD responses were measured for all films at different pulse voltages. For the 27 and 18 nm thick films, the capacitor radius studied was 12.5 μm, while for the 10 and 5 nm thick $Al_{0.72}Sc_{0.28}N$, the capacitor radius was reduced to 5 μm to stay within the current compliance limits of the ferroelectric tester beyond which a stable pulse voltage could not be applied to the sample. Figure 4 shows the current–time (I–t) responses of the 5 nm thick ferroelectric capacitor to a PUUNDD waveform with different pulse voltages and the resulting switched

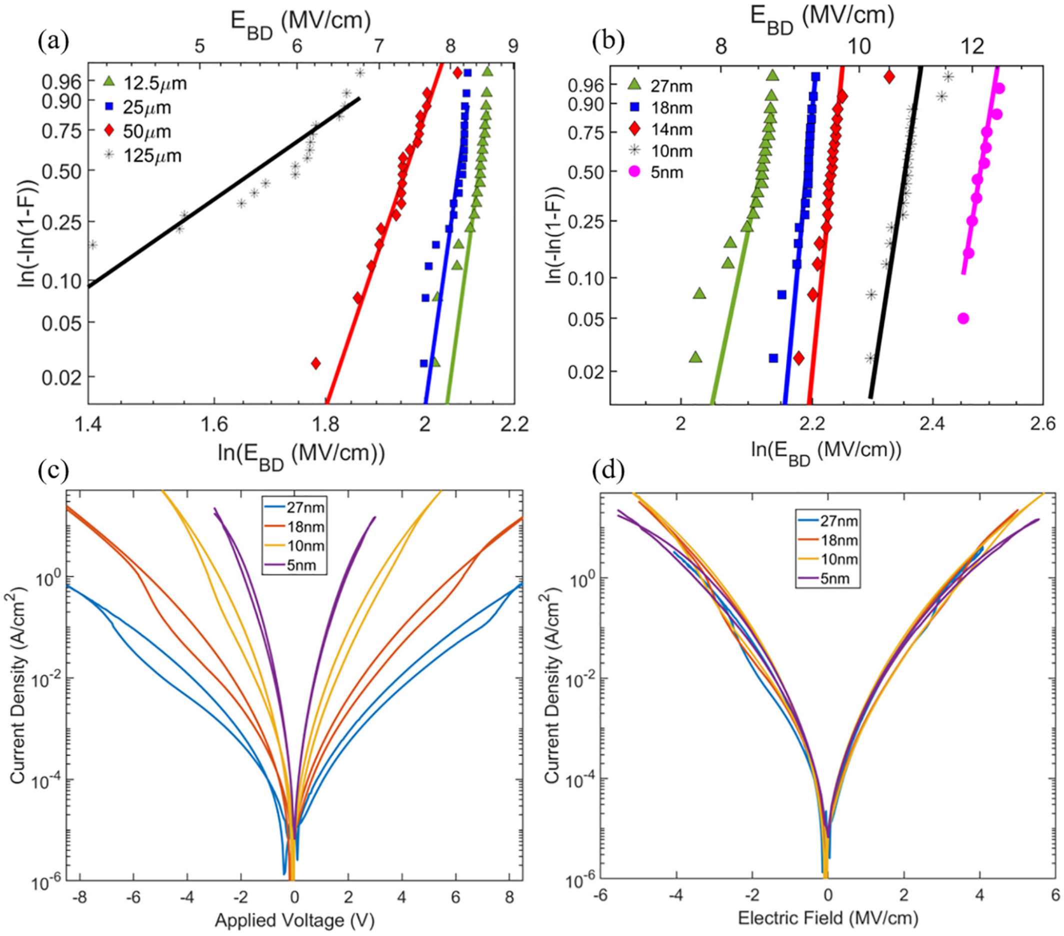

FIG. 3. (a) Weibull analysis of the electric breakdown field for 27 nm thick $Al_{0.72}Sc_{0.28}N$, where the capacitor radius is varied from 12.5 to 125 μm. (b) Weibull analysis of the electric breakdown field for a 12.5 μm radius capacitor where the film thickness is varied from 27 to 5 nm. Quasi-DC I–V hysteresis measurements of 12.5 μm radius capacitors as a function of thickness. (c) Current density of 27, 18, 10, and 5 nm thick $Al_{0.72}Sc_{0.28}N$ films as a function of voltage. (b) Current density of 27, 18, 10, and 5 nm thick $Al_{0.72}Sc_{0.28}N$ films as a function of electric field.

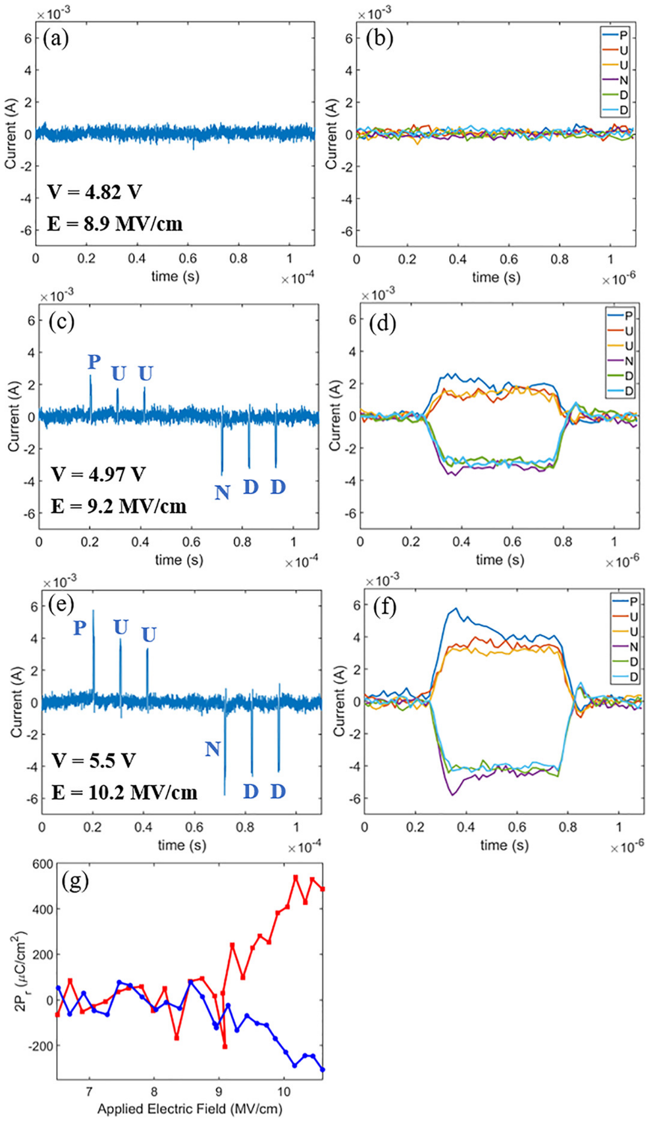

FIG. 4. Current vs time and polarization vs electric field responses of a 5 nm thick, 5 μm radius $Al_{0.72}Sc_{0.28}N$ ferroelectric capacitor to the 500 ns PUUNDD waveform shown in Fig. S3(c). (a) Full time response to a 4.82 V pulse. (b) PUUNDD capacitor currents from (a) overlaid in time. The voltage pulse is applied at t = 0.2 μs and has a rise time of 135 ns. Ferroelectric switching is not observed. (c) Full time response to a 4.97 V pulse. (d) PUUNND capacitor currents from (c) overlaid in time where the onset of ferroelectric switching with measurable polarization is first observed. (e) Full time response to a 5.5 V pulse corresponding to an electric field where a larger polarization is observed in (g). (d) PUUNND capacitor currents from (c) overlaid in time. (g) Switched polarization ($2P_r$) vs pulse amplitude used to estimate an E_C of 9.2 MV/cm. The blue trace corresponds to switching from metal polar to nitrogen polar, which provides a better estimate of the ferroelectric switched polarization.

polarization ($2P_r$) vs applied electric field. The capacitor current vs time in response to a pulsed voltage of 4.82 V is shown in Figs. 4(a) and 4(b), which is the highest voltage at which no ferroelectric switching current is observed. Ferroelectric switching with a measurable polarization is first observed at a voltage of 4.97 V as shown in Fig. 4(c), and this is utilized to estimate an E_C of 9.2 MV/cm for 500 ns pulse excitation. Figure 4(d) shows an overlay of the capacitor current in response to each pulse, where the 500 ns voltage pulse is applied at t = 0.2 μs. As shown in Fig. 4(d), the current in response to the P and N pulses is larger than those of the U and D pulses, resulting in a measurable polarization at an applied field of 9.2 MV/cm, as shown in Fig. 4(g). Figures 4(e) and 4(f) show the same I–t responses for a pulse voltage of 5.5 V, which corresponds to a field of 10.2 MV/cm. It can also be seen in Fig. 4(f) that the ferroelectric switching for the N pulse occurs more rapidly than for the P pulse due to $|E_C^+| > |E_C^-|$. Figure S5 shows the current responses to the P and N pulses overlaid in time with the measured capacitor voltage. The pulse voltage has a rise/fall time of 135 ns. The peak in the ferroelectric switching current occurs 60 ns after the pulse reaches its maximum voltage. The capacitor suffered electric breakdown at a voltage/field of 7.6 V/14.1 MV/cm. The PUUNDD or PUND capacitor responses for the 27, 18, and 10 nm $Al_{0.72}Sc_{0.28}N$ materials are provided in the supplementary material. From these data, we calculate the E_C of $Al_{0.72}Sc_{0.28}N$ when excited by a 500 ns pulse to be 5.6, 7.0, and 9.0 MV/cm for the 27, 18, and 10 nm films, respectively. Similar to prior PUND studies[14] in thicker AlScN materials, the $2P_r$ is less impacted by leakage for negative applied fields corresponding to the blue traces in the $2P_r$ vs electric field plots. Negative applied fields exceeding E_C switch the material from the metal polar (M-polar) state to the as-deposited nitrogen polar (N-polar) state. While the exact values of $2P_r$ are difficult to quantify precisely in the presence of the substantial leakage, no substantial reduction in the $2P_r$ with thickness scaling is observed, and the $2P_r$ remains above 170 $\mu C/cm^2$ for all thicknesses. For the 5.4 nm thick film, a $2P_r$ of 229–288 $\mu C/cm^2$ is measured for electric fields from 10.0 to 10.5 MV/cm from the blue trace in Fig. 4(g). The $2P_r$ is overestimated when compared to the well saturated values measured in thicker films[6,14] with similar Sc alloying, likely due to the higher coercive fields and correspondingly higher leakage currents observed with thickness scaling.

From the data presented, we observe that the E_C of $Al_{0.72}Sc_{0.28}N$ is dependent on the excitation frequency. Liu *et al.* found that the E_C of 100 nm thick, pulsed laser deposited (PLD) $Al_{70}Sc_{30}N$ was proportional to $f^{0.05}$ when measured between 50 Hz and 10 kHz.[24] The films reported in this work at various excitation frequencies follow this approximate trend $E_c \propto f^{0.05}$ and highlight the need to include the excitation frequency when comparing the V_C and E_C of various works. Figure 5 compares the E_C for the films reported in this paper with prior sub-20 nm $Al_{1-x}Sc_xN$ thickness scaling studies. In Fig. 5(a), the directly measured values are reported along with the measurement waveform and frequency. Figure 5(b) scales these measurements[22] to a common frequency of 10 kHz using $E_c \propto f^{0.05}$ for direct comparison. The E_C for all films increases when the thickness is reduced below 30 nm with a particularly sharp increase between 30 and 10 nm. The E_C of $Al_{1-x}Sc_xN$ decreases with decreasing c/a ratio, which can be altered via the Sc alloying ratio or film stress.[6] Gharavi *et al.* showed via transmission electron microscopy (TEM) that sputter deposited $Al_{0.64}Sc_{0.36}N$ on $\langle 111 \rangle$ platinum electrodes exhibited an ~9% tensile c-axis lattice strain and an ~5% a-axis lattice strain at the $Al_{1-x}Sc_xN$/Pt interface that relaxed over the first 10 nm of the film thickness.[18] Al has a similar lattice constant to Pt, and we expect the lattice mismatch strain here to be similar. We observed a similar trend in Fig. 1(c)

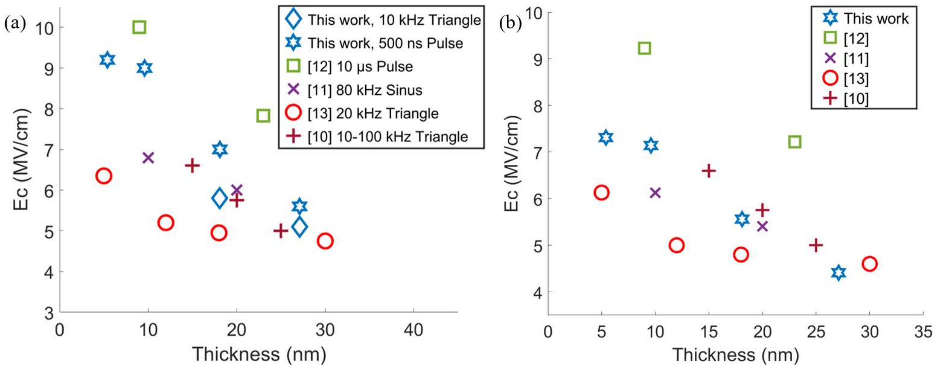

FIG. 5. (a) E$_C$ vs thickness of sub-20 nm Al$_{1-x}$Sc$_x$N thickness scaling studies. The values are reported as measured. (b) E$_C$ vs thickness of sub-20 nm Al$_{1-x}$Sc$_x$N thickness scaling studies with the values normalized to a 10 kHz excitation frequency.[22]

where the average c-axis lattice spacing increases from 5.01 to 5.07 Å as the film decreases from 27 to 5.4 nm thickness, indicating the thinner films have a larger c/a ratio and, thus, are expected to have a larger E$_C$. Beyond 30 nm thickness, the bottom 10 nm of the film, which is in high in-plane compressive stress, is a small part of the total film thickness, and the E$_C$ has a weak dependence on thickness. Once the film is thinned below 20 nm, however, the Al$_{1-x}$Sc$_x$N near the Al bottom electrode interface becomes a significant fraction of the total film thickness, leading to a rapid rise in the E$_C$. The thinnest films reported in this work can only be switched at thicknesses below 20 nm due to the corresponding rise in E$_{BD}$ with decreasing thickness. When scaling from 9.6 to 5.4 nm, we observe only a small increase in the c-axis in Fig. 2(c) and a correspondingly small increase in the E$_C$ in Fig. 5. The large E$_C$ in the thinnest films limits the ability to scale the V$_C$ through thickness scaling and suggests a bottom electrode with a better lattice match to Al$_{1-x}$Sc$_x$N such as Hf[25] (a = 3.2 Å), Zr[26,27] (a = 3.23 Å), or Sc (a = 3.31 Å), is a more effective approach to reduce the stress in the first 10 nm of film growth. While the Al and Al$_{1-x}$Sc$_x$N deposition processes utilized in this work are fully post-CMOS compatible, the sapphire substrates utilized to template the Al are not. Thus, future work will explore post-CMOS compatible seed materials for the Al, such as titanium (Ti), which can be sputter deposited *in situ* with the Al-Al$_{1-x}$Sc$_x$N-Al ferroelectric capacitor structures.

In summary, we have explored the thickness scaling of ferroelectric Al$_{0.72}$Sc$_{0.28}$N sputter deposited on Al electrodes down to 5.4 nm. The films exhibit high c-axis orientation with XRD rocking curve FWHM of AlScN (0002) ranging from 3.52° to 4.44°. The XRD shows that the average c-axis lattice constant increases with decreasing thickness, resulting in thinner films having an increased c/a ratio and a larger E$_C$. The E$_{BD}$ is observed to increase with decreasing film thickness. The 5.4 nm thick Al$_{0.72}$Sc$_{0.28}$N film showed ferroelectric switching at a voltage of 5.5 V when excited by a 500 ns square pulse and a switching speed of 60 ns.

See the supplementary material for additional information regarding XRR fitting of film thickness, Al$_{0.72}$Sc$_{0.28}$N XRD ω scans, 10 kHz and 100 kHz J–E hysteresis loops, the PUND and PUUNDD waveforms used to excite the Al$_{0.72}$Sc$_{0.28}$N ferroelectric capacitors, and the 27 nm, 18 nm, and 10 nm capacitor responses to the PUND and PUUNDD waveforms.

This work was supported by the Semiconductor Research Corporation (SRC) under Grant No. HR00112090046. The deposition, patterning, and characterizations of Al$_{1-x}$Sc$_x$N were performed at the Singh Center for Nanotechnology, supported by the NSF National Nanotechnology Coordinated Infrastructure Program (No. NNCI-1542153). Support for the electron microscope facility was also provided by the NSF through the University of Pennsylvania Materials Research Science and Engineering Center (MRSEC) (DMR-1720530) Sandia National Laboratories is a multimission laboratory managed and operated by National Technology and Engineering Solutions of Sandia, LLC, a wholly owned subsidiary of Honeywell International, Inc., for the U.S. Department of Energy's National Nuclear Security Administration under Contract No. DE-NA0003525. This paper describes objective technical results and analysis. Any subjective views or opinions that might be expressed in the paper do not necessarily represent the views of the U.S. Department of Energy or the United States Government.

AUTHOR DECLARATIONS

Conflict of Interest

The authors have no conflicts to disclose.

Author Contributions

J. X. Zheng and M. M. A. Fiagbenu contributed equally to this work.

Jeffrey X. Zheng: Conceptualization (supporting); Data curation (lead); Formal analysis (equal); Investigation (equal); Methodology (supporting); Writing – original draft (supporting). **Merrilyn Mercy Adzo Fiagbenu:** Data curation (lead); Formal analysis (supporting); Methodology (equal); Writing – review & editing (equal). **Giovanni Esteves:** Data curation (equal); Formal analysis (equal); Investigation (equal); Methodology (equal); Writing – review & editing (equal). **Pariasadat Musavigharavi:** Investigation (supporting); Methodology (supporting); Supervision (supporting); Writing – review & editing (equal). **Akhil Gunda:** Data curation (supporting). **Deep Jariwala:** Conceptualization (supporting); Methodology (supporting); Supervision (supporting); Writing – review & editing (equal). **Eric A. Stach:** Conceptualization (equal); Formal analysis (supporting); Funding acquisition (supporting); Methodology (equal); Project administration (supporting); Supervision (equal); Writing – review &

editing (equal). **Roy Harold Olsson III:** Conceptualization (lead); Formal analysis (equal); Funding acquisition (lead); Investigation (equal); Methodology (equal); Project administration (lead); Supervision (equal); Writing – original draft (lead); Writing – review & editing (equal).

DATA AVAILABILITY

The data that support the findings of this study are available from the corresponding author upon reasonable request.

REFERENCES

[1] H.-S. P. Wong and S. Salahuddin, Nat. Nanotechnol. **10**(3), 191 (2015).
[2] D. Ielmini and H.-S. P. Wong, Nat. Electron. **1**(6), 333 (2018).
[3] H. Cai, W. Kang, Y. Wang, L. A. De Barros Naviner, J. Yang, and W. Zhao, Appl. Sci. **7**(9), 929 (2017).
[4] H. Bae, T. Moon, S. G. Nam, K.-H. Lee, S. Kim, S. Hong, D.-H. Choe, S. Jo, Y. Lee, and J. Heo, in proceedings of IEEE Symposium on VLSI Technology and Circuits, IEEE, 2021.
[5] X. Liu, J. Ting, Y. He, M. M. A. Fiagbenu, J. Zheng, D. Wang, J. Frost, P. Musavigharavi, G. Esteves, K. Kisslinger, S. B. Anantharaman, E. A. Stach, R. H. Olsson III, and D. Jariwala, Nano Lett. **22**, 7690 (2022).
[6] S. Fichtner, N. Wolff, F. Lofink, L. Kienle, and B. Wagner, J. Appl. Phys. **125**(11), 114103 (2019).
[7] D. Drury, K. Yazawa, A. Zakutayev, B. Hanranan, and G. Brennecka, Micromachines **13**, 887 (2022).
[8] S. K. Ryoo, K. D. Kim, H. W. Park, Y. B. Lee, S. H. Lee, I. S. Lee, S. Byun, D. Shim, J. H. Lee, H. Kim, Y. H. Jang, M. H. Park, and C. S. Hwang, Adv. Electron. Mater. **8**(11), 2200726 (2022).
[9] D. X. Wang, J. Zheng, P. Musavigharavi, W. L. Zhu, A. C. Foucher, S. E. Trolier-McKinstry, E. A. Stach, and R. H. Olsson, IEEE Electron Device Lett. **41**(12), 1774 (2020).
[10] S. R. C. Mitchell, A. W. Walke, K. Banerjee, S. Mertens, X. Piao, M. Mao, K. Katcko, G. Vellianitis, M. van Dal, Y.-M. Lin, G. van den Bosch, R. Delhougne, and G. S. Kar, ACS Appl. Electron. Mater. **5**(2), 858–864 (2023).
[11] G. Schonweger, M. R. Islam, N. Wolff, A. Petraru, L. Kienle, H. Kohlstedt, and S. Fichtner, Phys. Rapid Res. Lett. **17**, 2200312 (2023).
[12] R. Mizutani, S. Yasuoka, T. Shiraishi, T. Shimizu, M. Uehara, H. Yamada, M. Akiyama, O. Sakata, and H. Funakubo, Appl. Phys. Express **14**(10), 105501 (2021).
[13] D. Wang, P. Wang, S. Mondal, M. Hu, D. Wang, Y. Wu, T. Ma, and Z. Mi, Appl. Phys. Lett. **122**, 052101 (2023).
[14] D. X. Wang, P. Musavigharavi, J. Zheng, G. Esteves, X. W. Liu, M. M. A. Fiagbenu, E. A. Stach, D. Jariwala, and R. H. Olsson, Phys. Rapid Res. Lett. **15**(5), 2000575 (2021).
[15] G. Esteves, T. R. Young, Z. Tang, S. Yen, T. M. Bauer, M. D. Henry, and R. H. Olsson III, Appl. Phys. Lett. **118**(17), 171902 (2021).
[16] Y. R. Koh, J. Shi, B. Wang, R. Hu, H. Ahmad, S. Kerdsongpanya, E. Milosevic, W. A. Doolittle, D. Gall, Z. Tian, S. Graham, and P. E. Hopkins, Phys. Rev. B **102**, 205304 (2020).
[17] B. H. Toby and R. B. von Dreele, J. Appl. Crystallogr. **46**(2), 544–549 (2013).
[18] N. Kurz, A. Ding, D. F. Urban, Y. Lu, L. Kirste, N. M. Feil, A. Žukauskaitė, and O. Ambacher, J. Appl. Phys. **126**, 075106 (2019).
[19] Q. Wen, X. Wei, F. Jiang, J. Lu, and X. Xu, Materials (Basel) **13**(12), 2871 (2020).
[20] P. S. M. Gharavi, A. C. Meng, D. Wang, J. Zheng, A. C. Foucher, R. H. Olsson III, and E. A. Stach, J. Phys. Chem. C **125**(26), 14394–14400 (2021).
[21] M. Akiyama, T. Kamohara, K. Kano, A. Teshigahara, Y. Takeuchi, and N. Kawahara, Adv. Mater. **21**, 593 (2009).
[22] S. Yasuoka, T. Shimizu, A. Tateyama, M. Uehara, H. Yamada, M. Akiyama, Y. Hiranaga, Y. Cho, and H. Funakubo, J. Appl. Phys. **128**, 114103 (2020).
[23] X. Liu, J. Zheng, D. Wang, P. S. M. Gharavi, E. A. Stach, R. H. Olsson III, and D. Jariwala, Appl. Phys. Lett. **118**, 202901 (2021).
[24] C. Liu, Q. Wang, W. Yang, T. Cao, L. Chen, M. Li, F. Liu, D. K. Loke, J. Kang, and Y. Zhu, paper presented at IEEE Electron Devices Meeting, 2021.
[25] G. Coiffard, M. Daal, N. Zobrist, N. Swimmer, S. Steiger, B. Bumble, and B. A. Mazin, Supercond. Sci. Technol. **33**, 07LT02 (2020).
[26] C.-C. Kuo, C.-H. Lin, J.-T. Chang, and Y.-T. Lin, Coatings **11**, 7 (2020).
[27] A. Singh, P. Kuppusami, R. Thirumurugesan, R. Ramaseshan, M. Kamruddin, S. Dash, V. Ganesan, and E. Mohandas, Appl. Surf. Sci. **257**, 9909–9914 (2011).